

# Magnetohydrodynamic equilibrium and stability of rotating plasmas in a mirror geometry

A. Y. Aydemir

*Institute for Fusion Studies*

*The University of Texas at Austin*

*Austin, TX 78712 USA*

(Dated: September 16, 2004)

## Abstract

A systematic study of equilibrium and stability of rotating plasmas in a mirror geometry is presented. At supersonic azimuthal rotation velocities, centrifugal forces lead to equilibria with nearly detached plasmas, where the plasma mass concentrates at the mirror center. However, isolation of the plasma from the ends is not complete due to high parallel thermal conduction. Temperature remains a flux function, connecting the centrifugally confined region to the end points. Rotation shear is found to be strongly stabilizing for the interchange (flute) modes, as demonstrated in earlier works. However, all configurations studied to date with various rotation profiles are found to be linearly unstable to other ideal magnetohydrodynamic (MHD) modes. Thus, it is unlikely that these centrifugally detached states can be accessed within ideal MHD.

## I. INTRODUCTION

Mass flows are a common feature of many magnetic confinement schemes. Whether they are self-consistently generated, as in the shear-flows that play an important role in reduced turbulent transport in tokamaks, or result from an external momentum source such as neutral beams, they have a significant impact on equilibrium and stability of confined plasmas. Thus, their effects have been examined, both analytically and numerically, in a number of studies. See, for example, Hameiri[1], and Bhattacharjee[2], and the references therein.

In addition to these “incidental” flows, which arise spontaneously or merely as a side effect, large-scale flows that are designed to be an integral part of confinement have also been considered from very early on[3]. More recently, there has been a revival of interest in systems where the forces generated by strong flows play a role comparable to that of the magnetic field in confining the plasma. This idea has been explored, mostly in the context of a centrifugally confined rotating mirror plasma, by Hassam and coworkers in a series of articles examining equilibrium, stability, and transport in such a device[4–8]. Their work has produced mostly favorable stability results and clearly demonstrated stabilization of the interchange (flute) modes by flow-shear. However, imposed symmetries in some of those calculations may have excluded other unstable modes. Also an apparent absence of a clear separation of the effects of diffusive transport from MHD (magnetohydrodynamics) may have led to some misleading results. One of the goals of this work is to do a comprehensive study of linear MHD stability in such systems, with no symmetry assumptions, and clearly separated MHD and transport time scales. Obviously, possible nonlinear stabilization of these modes is an important topic also, as demonstrated in some of the Maryland work, which tends to show a benign evolution towards a neighboring equilibrium state. We intend to look at nonlinear stability in a future work.

Another source of interest in these configurations with strong flows is their possible role as relaxed, or self-organized, states that arise in some variational studies[9, 10]. As we will

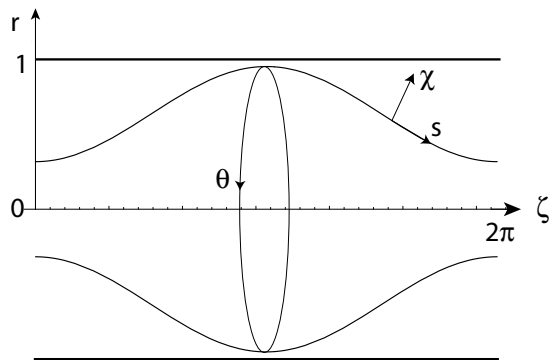


FIG. 1: Geometry and the coordinate systems.

see below, centrifugally-confined “detached states” observed in our equilibrium calculations are found to be ideal-MHD unstable; therefore, they cannot be manifestations of a relaxed state. However, since the Yoshida-Mahajan states seem to require a two-fluid Hall MHD model as a prerequisite, it is not clear if our single-fluid results are relevant to their work.

The next section introduces the simplified geometry and model equations used in this study.

## II. GEOMETRY AND MODEL EQUATIONS

The rotating mirror is modeled by a straight cylinder with a perfectly conducting wall and periodically identified ends. The ambient fields are assumed to be produced by external currents. The geometry of the problem and the coordinate systems used are shown in Fig. 1. The numerical calculations are done in the cylindrical  $(r, \theta, \zeta)$  coordinates, with the “toroidal” angle  $\zeta$  related to the usual axial coordinate  $z$  through  $z = R_0\zeta$ , where  $R_0$  is taken to be unity in this work. A flux-coordinate system,  $(\chi, \theta, s)$ , used in the equilibrium discussion, is also shown.

The single fluid MHD equations are written in the following non-dimensional form:

$$\frac{\partial \rho}{\partial t} + \nabla \cdot (\rho \mathbf{u}) = 0 \quad (1)$$

$$\rho \frac{\partial \mathbf{u}}{\partial t} + \rho (\mathbf{u} \cdot \nabla) \mathbf{u} = \mathbf{J} \times \mathbf{B} - \nabla p, \quad (2)$$

$$\frac{\partial \mathbf{A}}{\partial t} = \mathbf{u} \times \mathbf{B} - \eta \mathbf{J}, \quad (3)$$

$$\frac{\partial p}{\partial t} + (\mathbf{u} \cdot \nabla) p = -\gamma p \nabla \cdot \mathbf{u} + \kappa_{\perp} \nabla^2 p + \kappa_{\parallel} \nabla_{\parallel}^2 (p/\rho), \quad (4)$$

$$\mathbf{B} = \nabla \times \mathbf{A}, \quad \mathbf{J} = \nabla \times \mathbf{B}. \quad (5)$$

The variables have their usual meanings. Time is normalized to the Alfvén time  $\tau_A = a/v_A$ , where  $a$  is the cylinder radius, and  $v_A = B_0/\sqrt{\mu_0 \rho_0}$  is the Alfvén velocity defined in terms of a characteristic field strength  $B_0$  and mass density  $\rho_0$ . In equilibrium calculations, parallel thermal conduction is treated iteratively to ensure that temperature remains a flux function. Perpendicular transport coefficients, for both equilibrium and linear stability calculations, are taken to be small enough to provide more than adequate time-scale separation between MHD and transport. Typically, we have  $\eta \sim \kappa_{\perp} \sim O(10^{-5})$ , with an additional numerical viscosity coefficient of  $O(10^{-4})$ . The linear stability calculations are truly linear in the sense that the background fields are frozen in time as we solve for the perturbed quantities as an initial-value problem.

Since the field lines intersect the perfectly conducting wall, *i.e.*  $B_r(r=1, \theta, \zeta) \neq 0$ , no-slip boundary conditions are imposed on velocity in order to avoid parallel electric fields:  $\mathbf{u} = 0$  at the wall. When calculating a family of equilibria with increasing rotation frequency but with a fixed rotation-shear profile, we also hold the net toroidal flux and plasma  $\beta$  constant.

The numerical code used here is a modification of an older one originally discussed in Ref. [11]. It has gone through many improvements over the years, but many of the algorithmic details can be found there. Briefly, it uses finite differences in the radial direction and Fourier expansions in the other (periodic) coordinates  $\theta$ , and  $\zeta$ . Here we use 128 radial grid points. The mirror equilibria are described using a spectral expansion with  $m = 0$ , and  $0 \leq n \leq 9$ , where  $m, n$  are the poloidal (azimuthal) and toroidal (axial) mode numbers, respectively. In the linear calculations for a given mode number  $m > 0$ , we use a toroidal

expansion with  $-9 \leq n \leq 9$ . The simple  $\theta$ -pinch calculations require only the  $m = n = 0$  component to describe the equilibrium, and a single  $m, n$  pair for the linear mode.

In the next section, after a general discussion of MHD equilibrium in rotating mirrors, numerically found detached states are introduced.

### III. EQUILIBRIUM AND DETACHED STATES

As stated in the Introduction, MHD equilibria with mass flows have been studied extensively. More recent discussions relevant to the present topic can be found in Ellis, *et al.*[7] and Hazeltine, *et al.*[12]. Below, we review some of the important features of equilibria in centrifugally confined mirrors.

#### A. General properties of rotating mirror equilibria

Assuming azimuthal symmetry ( $\partial/\partial\theta = 0$ ), a general mirror field in the geometry of Fig. 1 can be written in terms of  $A_\theta$  alone:

$$\mathbf{B} = \nabla \times rA_\theta \nabla\theta = \nabla\chi \times \nabla\theta, \quad (6)$$

where  $\chi \equiv rA_\theta$  is the toroidal flux function. (We will refer to  $\theta$  and  $\zeta$  directions as the poloidal and toroidal directions, respectively.) Assuming steady-state fields and a “general” Ohm’s law of the form  $\mathbf{E} = -\mathbf{u} \times \mathbf{B} + \mathbf{b}E_\parallel = -\nabla\phi$  leads to

$$u^\chi = 0, \quad (7)$$

$$u_\theta = r\Omega(\chi, s), \quad \Omega \equiv \partial\phi(\chi, s)/\partial\chi, \quad (8)$$

$$E_\parallel = -\partial\phi(\chi, s)/\partial s. \quad (9)$$

The first equation above merely states that there can be no equilibrium flows across flux surfaces, as expected. The second equation gives the poloidal rotation velocity in terms of a general rotation frequency  $\Omega = \Omega(\chi, s)$ , which, because of an assumed parallel electric field, can vary along the field lines. We see that, in non-ideal MHD ( $E_\parallel \neq 0$ ), the parallel and

perpendicular dynamics are intimately connected, *i.e.*, the rotation velocity  $u_\theta$  and  $E_\parallel$  are not independent, a point that was also pointed out by Hazeltine, *et al.*[12]. In fact, a rotation profile that is sheared along the direction of the field is consistent with a steady-state field only if there is a compensating parallel electric field that prevents the twisting of the field lines.

In general, the velocity field can have a parallel component also:  $\mathbf{u} = r^2\Omega\nabla\theta + \mathbf{b}u_\parallel$ . However,  $u_\parallel$  is not quite arbitrary; mass continuity,  $\nabla \cdot (\rho\mathbf{u}) = 0$ , leads to

$$\rho u_\parallel / |B| = F(\chi), \quad (10)$$

where  $F$  is an arbitrary flux function. Thus, if  $u_\parallel$  vanishes anywhere on a flux surface, it has to be zero everywhere on that surface.

Finally, the momentum equation (with  $u_\parallel = 0$ ) leads to

$$(1/r^2)\Delta^*\chi = (1/2)\rho\Omega^2\partial r^2/\partial\chi - \partial p/\partial\chi, \quad (11)$$

$$\partial p/\partial s = (1/2)\rho\Omega^2\partial r^2/\partial s. \quad (12)$$

The first equation, which gives the force-balance condition across flux surfaces, is the equivalent of a ‘‘Grad-Shafranov’’ equation for this geometry. The second one states that the parallel component of the centrifugal force (the right-hand side) has to be balanced by a parallel pressure gradient; thus, in general, the pressure and mass density are not flux functions in the presence of flows.

Analytically it is difficult to make further progress with Eq. 11. However, the parallel force-balance equation (Eq. 12) can be integrated if we assume: a)  $E_\parallel = 0$ , which leads to  $\Omega = \Omega(\chi)$ , and b) fast parallel thermal conduction, giving  $T = T(\chi)$ . Then the result can be put in the form

$$\rho(\chi, s) = \rho_0 \exp(-(r_0^2 - r^2)/w^2), \quad (13)$$

where  $\rho_0 \equiv \rho(\chi, s = 0)$ ,  $r_0 \equiv r(\chi, s = 0)$ ,  $w = r/M_s$ , the Mach number  $M_s = u_\theta/c_s$ , and the sound speed  $c_s = \sqrt{\gamma p/\rho}$ . Defining  $s = 0$  to be at the symmetry plane  $\zeta = \pi$ , we see that the mass density decays exponentially as we go along a field line towards the mirror

throats ( $s > 0$ ) only if  $M_s \gg 1$ , *i.e.* the centrifugal confinement becomes effective only for supersonic rotations.

Although  $M_s \gg 1$  is required for centrifugal confinement, there is obviously an upper limit on how fast the rotation can be. Integrating the radial force-balance equation at the mid-plane ( $\zeta = \pi$ ),

$$\partial P / \partial r = r \rho \Omega^2, \quad (14)$$

where  $P \equiv p + B_\zeta^2/2$ , leads to an approximate upper bound on the rotation velocity,

$$u_\theta^2(a) < v_A^2(a) - c_s^2(0), \quad (15)$$

where  $v_A^2(a) \equiv B_\zeta^2(a)/\bar{\rho}$ ,  $c_s^2(0) \equiv \gamma p(0)/\bar{\rho}$ , and  $\bar{\rho}$  is a mean density. Above, we also assumed rigid-body rotation. Combining the upper and lower limits in one expression, we get

$$1 < M_s^2 < (1 - \beta_0)/\beta_0, \quad \beta_0 \equiv c_s^2(0)/v_A^2(a), \quad (16)$$

as a requirement for effective centrifugal confinement. Note that the upper bound is only  $M_s = 3$  for  $\beta_0 = 10\%$ .

Next we discuss numerically found equilibria and detached states with strong flows.

## B. Detached states

Two-dimensional mirror equilibria with rotation can be found by solving the Grad-Shafranov equation, Eq. 11, for the flux function  $\chi$  using appropriate source terms. However, we find it more convenient to solve Eqs. (1-5) as an initial/boundary value problem and relax to a two-dimensional rotating equilibrium, starting from a one-dimensional  $\theta$ -pinch configuration. The initial step in this relaxation process is a mirror equilibrium without rotation, an example of which is shown in Fig. 2.

After a static mirror equilibrium is found, rotation with a given profile is driven using a source term in the momentum equation:

$$\frac{\partial \mathbf{u}}{\partial t} = \mathbf{F} - \frac{1}{\tau_\Omega} (\mathbf{u} - \mathbf{u}_\Omega), \quad (17)$$

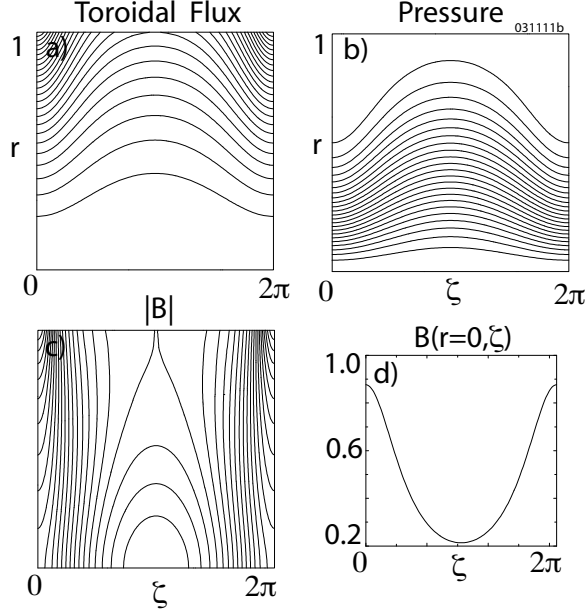


FIG. 2: A static mirror equilibrium ( $\Omega = 0$ ). a) Toroidal flux function in the  $(r, \zeta)$  plane, b) pressure, c) mod-B contours, d) mod-B along the symmetry axis. The mirror ratio is approximately 4.5 here.

where the time constant  $\tau_\Omega \sim 10$ , and  $\mathbf{F}$  represents the remaining terms of Eq. 2. The desired rotation velocity is specified as  $\mathbf{u}_\Omega = r^2 \Omega \nabla \theta$ , where  $\Omega = \Omega_0 f(x)$ ,  $x \equiv \chi/\chi_{max}$ , and  $f(x)$  is a flux function determining the profile. A couple of different parametrizations have been used for  $f(x)$ :

$$f_1(x) = (1 - \exp(-(1 - x^2)/w^2))/(1 - \exp(-1/w^2)), \quad (18)$$

$$f_2(x) = (1 - x^\lambda)^2. \quad (19)$$

Figure 3 shows some of the typical profiles used in this work. Curves (a-c), with  $f = f_1(x)$ , represent low to moderate rotation-shear, whereas (d), using  $f = f_2(x)$ , shows a profile with a very high degree of shear.

We typically generate a family of rotating equilibria by incrementally increasing the frequency with a fixed profile until the radial force-balance limit is reached. An example with medium rotation-shear, corresponding to the profile of Fig. 3(b) at  $\Omega_0 = 0.73$ , is shown in Fig. 4. The plasma  $\beta$  is 10%, where we use the somewhat unorthodox definition  $\beta \equiv 2 \langle p \rangle \langle 1/B^2 \rangle$ , with the brackets denoting volume averages. Also using the definition for a mean Mach number,  $\overline{M}_s \equiv a\Omega_0/v_A\beta^{1/2} = \Omega_0/\beta^{1/2}$ , we have for this equilibrium  $\overline{M}_s = 2.3$ .

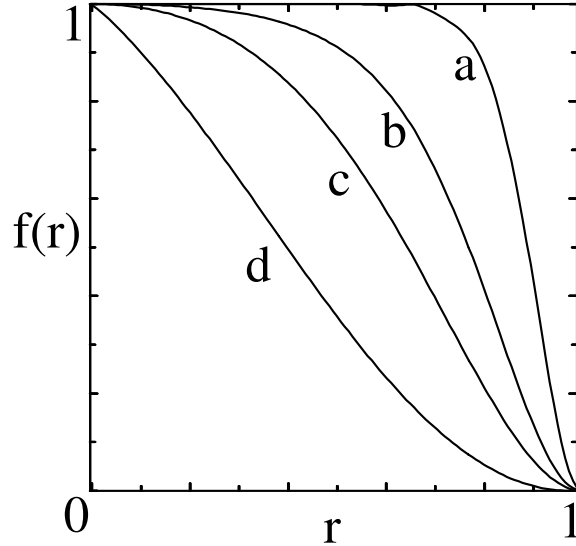


FIG. 3: Typical rotation frequency profiles used in this work. Curves (a-c) correspond to  $f = f_1(x)$  of Eq. 18, with  $w = 0.273, 0.546, 1.09$ , respectively. Curve (d) uses  $f = f_2(x)$  of Eq. 19, with  $\lambda = 0.6$ . Note that the curves show  $f = f(x(r))$ , not  $f(x)$ , where  $x = \chi/\chi_{max}$ .

The actual rotation frequency for the fluid, calculated as  $\Omega = u_\theta/r$ , is shown in Fig. 4 (a). Due to line-tying, the fluid in the open-flux regions where the field lines intersect the conducting wall does not rotate; elsewhere we see that  $\Omega$  is a flux function. The pressure contours in Fig. 4 (b), however, clearly show that, in trying to balance the centrifugal forces along the curved lines of the mirror field, the plasma pressure has become nonuniform along the flux surfaces. Figure 4 (d) has the flux and temperature contours superimposed over each other, showing that the temperature is still a flux function,  $T = T(\chi)$ . As expected, the mass density exhibits the most dramatic response to centrifugal forces by concentrating in a ring-like structure encircling the mirror axis, centered at the symmetry plane between the mirrors, as seen in Fig. 4 (e). This detached plasma is confined along the field lines by centrifugal forces only, while the magnetic field still provides the perpendicular confinement. Note, however, parallel thermal conduction still connects the end-points to the center, the detached region, since we still have  $T = T(\chi)$ ; thus, mass, but not energy, confinement is enhanced by rotation.

A second example, this time with higher shear, is shown in Fig. 5. The rotation profile [Fig. 3(d)] is  $\Omega = \Omega_0 f_2(x(r))$ , where  $f_2$  is given by Eq. 19 with  $\lambda = 0.6$ . A sequence of

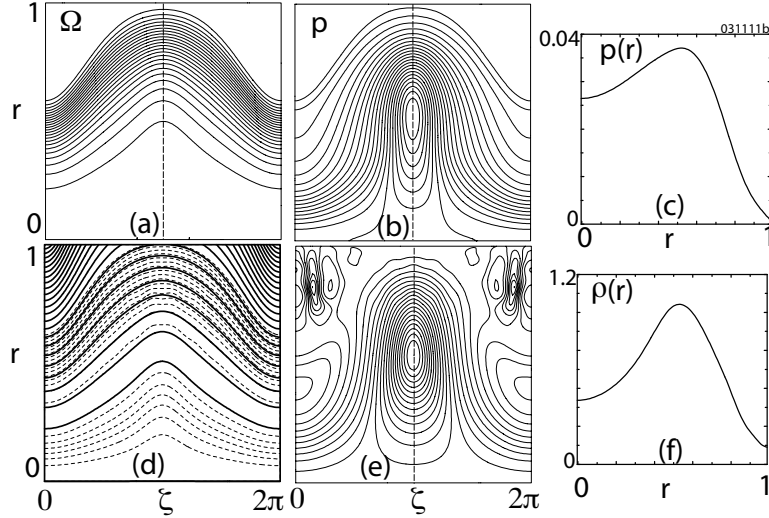


FIG. 4: A rotating mirror equilibrium with medium rotation shear. The rotation profile is that of Fig. 3(b) ( $f_1$  of Eq. 18 using  $w = 0.546$ ), with  $\Omega_0 = 0.73$ . a) Rotation frequency,  $\Omega \equiv u_\theta(r, \zeta)/r$ , contours in the  $(r, \zeta)$  plane, b) pressure contours, c) pressure at the symmetry plane (along the dashed line in (b)), d) flux (solid lines) and temperature (dashed lines) contours superimposed, e) mass density contours, f) density at the symmetry plane. Note that the temperature is a flux function, whereas the mass density exhibits a clearly detached region at the center nearly disconnected from the mirror throats.

equilibria with increasing rotation frequencies is shown, clearly exhibiting the development of a well-detached plasma at the center. The plasma  $\beta$  is again 10%, and at  $\Omega_0 = 1.3$ , the Mach number is  $\overline{M}_s = 4.1$ . Because of the higher shear, detachment starts near the mirror axis and eventually (for  $\Omega_0 > \sim 1$ ) leads to one of the best examples of detached states seen in this work. Again, the temperature remains a flux function, following the slight outward displacement of the flux with increasing centrifugal forces. The final states shown here and in the previous equilibrium of Fig. 4 are nearly at the critical radial force-balance point where any further increase in the centrifugal forces cannot be balanced by the Lorentz force, causing the plasma to “fly apart,” or become wall-confined.

All equilibrium calculations exhibit irregular mass density structures outside the last closed flux surface. In this region, connected to the wall by thermal conduction along open field lines, the plasma pressure is zero since the temperature  $T = T_{wall} = 0$ . Thus, there are no sound waves that would otherwise tend to remove the density gradients along the field lines. (Recall that there is also no rotation in this region.)

The examples shown above, and numerous others found in various parameter regimes,

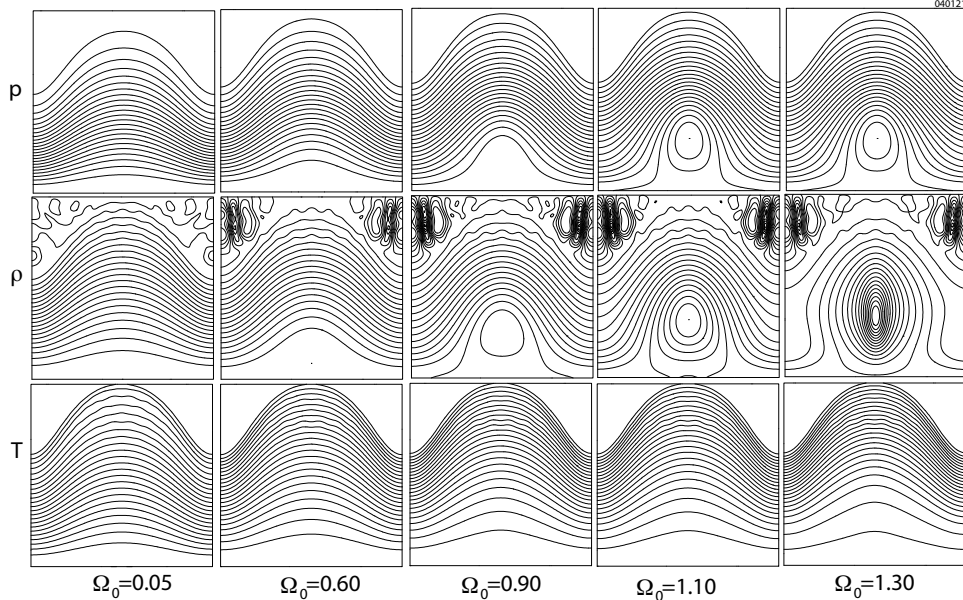


FIG. 5: A rotating mirror equilibrium with high rotation shear. The rotation profile is that of Fig. 3(d) ( $f_2$  of Eq. 19 with  $\lambda = 0.6$ .) The pressure, density, and temperature contours in the  $(r, \zeta)$  plane are shown for a family of equilibria with increasing rotation frequency.

provide convincing evidence for the possible efficacy of the centrifugal confinement concept in rotating mirrors, at least in the context of ideal MHD. Although these detached states were obtained using an initial/boundary value relaxation process, azimuthal symmetry imposed on the calculations, and other constraints placed in the parallel direction (*e.g.* continual removal of non-rotational kinetic energy) possibly excluded from the system dangerous instabilities that may make these states inaccessible. Therefore, in the next section we examine their MHD stability.

#### IV. LINEAR STABILITY

As in the equilibrium calculations above, linear stability is treated as an initial/boundary value problem also. A disadvantage of this approach is that usually only the fastest growing mode can be found. However, since our goal here is to determine the stability of detached states, without necessarily finding the full spectrum of unstable modes, our methods will suffice. They also have the advantage of avoiding some of the complications of an eigenvalue approach in the presence of strong rotation. In the next subsection, we examine stability

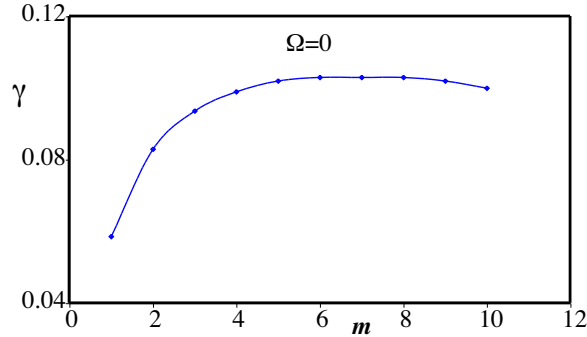


FIG. 6: The interchange (flute) mode growth rates for the non-rotating mirror equilibrium of Fig. 2.

in a full mirror geometry. Later we will look at stability in simpler  $\theta$ -pinch equilibria with rotation in order to shed some light on the mirror geometry results.

### A. Mirror stability

Using spectral methods, an eigenfunction with a given poloidal mode number  $m$  is expanded in the form

$$p_m(r, \zeta, t) = \sum_{n=-N}^{n=N} p_{mn}(r, t) e^{in\zeta}, \quad (20)$$

with typically  $N \sim 10$ . The background equilibrium fields have similar expansions, constant in time and with  $m = 0$ .

As expected, non-rotating mirror equilibria are found to be unstable to ideal interchange (flute) modes, as shown for a typical equilibrium in Fig. 6. Theoretically, all mode numbers are unstable, with the growth rate scaling as  $\gamma \sim m^{1/2}$  for  $m \sim O(1)$  and asymptotically approaching a constant for  $m \gg 1$ , in approximate agreement with the results of Fig. 6. Because of various dissipative terms in our model, we find that the numerical growth rates tend to deviate from this scaling towards the upper end of the range of modes considered.

The pressure eigenfunction for the most unstable mode,  $m = 6$ , is shown in Fig. 7. Radial variation of some of the components (with  $n = 0 \dots 5$ ) are shown in Fig. 7(a). A curious feature of these modes is that the number of radial nodes (zero-crossings) is equal to the toroidal mode number  $n$ .

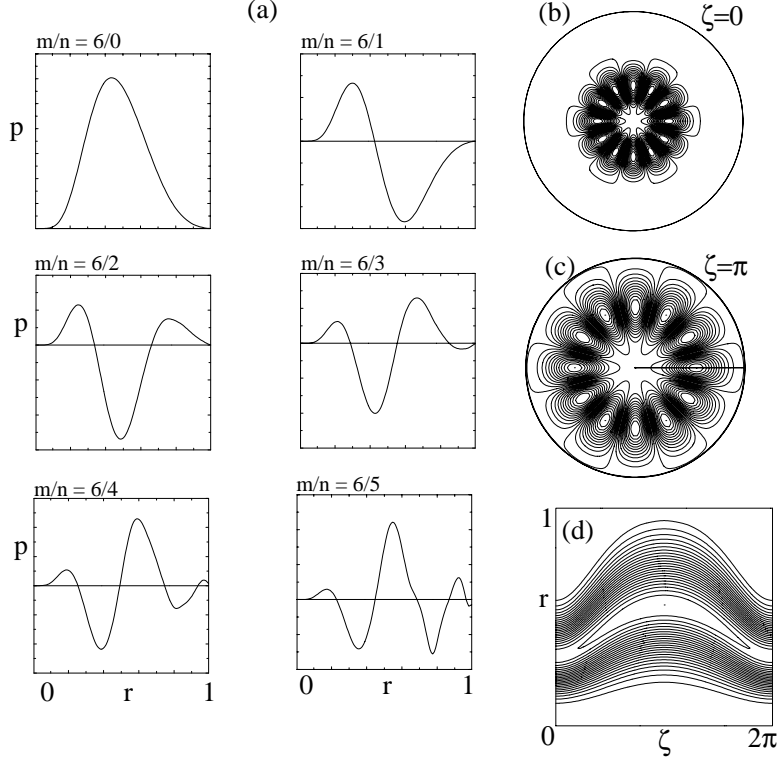


FIG. 7: The pressure eigenfunction for  $m = 6$ . a)  $n = 0, 1, \dots, 5$  components, as a function of radius. Note that the number of radial nodes is equal to the toroidal mode number  $n$ . b) Contours of the eigenfunction in the  $\zeta = 0$  poloidal plane, c) Contours at  $\zeta = \pi$ , the symmetry plane, d) Contours in the  $(r, \zeta)$  plane. Note that there is no variation along the field lines, as expected of a flute mode.

Figures 7(b,c) show the eigenfunction at the  $\zeta = 0$ , and  $\zeta = \pi$  planes, respectively, showing the  $m = 6$  pairs of lobes, characteristic of interchange modes, and the lack of variation along the field lines. The last figure (d) shows the contours in the  $(r, \zeta)$  plane, again clearly demonstrating that  $(\mathbf{B}_0 \cdot \nabla)p_1 = 0$  for this mode.

Having established the main features of the interchange mode in this geometry, we next look at how they are modified in the presence of strong rotation, using various rotation profiles.

Rotation itself, without any shear, has a destabilizing influence on the interchange modes. Assuming a rigid body rotation (completely shear-free) and transforming to a rotating frame of reference, it is easy to see that the centrifugal forces merely act as an additional drive enhancing the growth rate. At sufficiently high  $\Omega$ , the effective “g” becomes  $u_\theta^2/r = r\Omega^2$ , leading to the scaling  $\gamma \sim (gk_\perp)^{1/2} \sim \Omega m^{1/2}$  for small  $m$ . The stabilizing effect, of course,

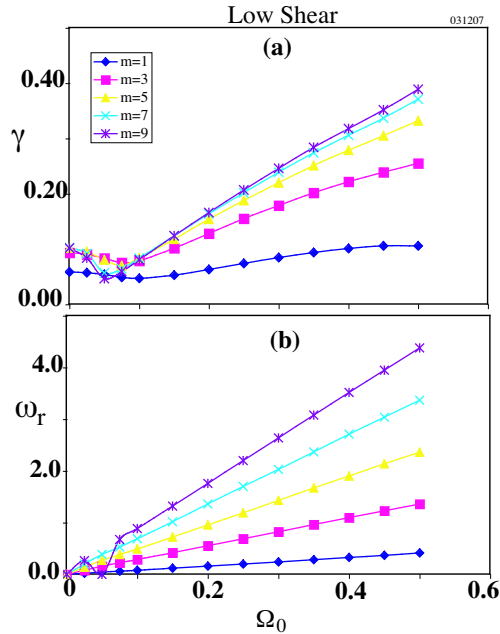


FIG. 8: The growth rate (a), and the real frequency (b), of the unstable modes as a function of rotation frequency for the low-shear profile (a) of Fig. 3. For clarity, only odd-numbered modes are shown. Note that the destabilizing effect of rotation dominates over shear-stabilization for  $\Omega_0 \geq 0.05$ .

comes from the shear in the profile, through its effect, for example, on the pressure “cells” of Figs. 7(b,c). Thus, the net effect of rotation on stability critically depends on the amount of shear present.

Starting with the low-shear profile (a) of Fig. 3, we see that rotation is quite destabilizing here, with the growth rates increasing as  $\gamma \sim \Omega_0$  for  $\Omega_0 \geq 0.1$ , as seen in Fig. 8(a). The initial decrease can be attributed to the influence of the narrow shear layer near the wall. Since the centrifugal confinement becomes effective (in modifying the density profile) only above  $\Omega \simeq 0.3$  for this profile, this minor effect on stability is not relevant. The modes tend to rotate with the fluid; thus, for the most part, the real frequency scales as  $\omega_r \sim m\Omega_0$ . However, at  $\Omega_0 = 0.05$ , the  $m = 9$  mode with the highest growth rate appears to have  $\omega_r \ll \Omega_0$ . More examples of these new “zero-frequency” modes will be seen below.

Using a profile with higher shear [Fig. 3(b)] leads to somewhat more encouraging stability results, as seen in Fig. 9. The increased shear has a pronounced stabilizing effect on all modes for approximately  $\Omega_0 \leq 0.2$ , beyond which the interchange modes reappear with

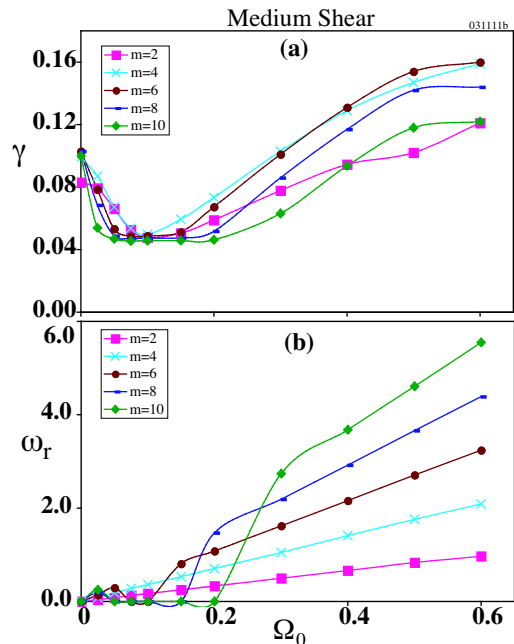


FIG. 9: The growth rate (a), and the real frequency (b), of the unstable modes as a function of rotation frequency for the medium-shear profile (b) of Fig. 3. Only even-numbered modes are shown.

large growth rates, and real frequencies that scale as  $\omega_r \sim m\Omega_0$ . However, for approximately  $0.05 \leq \Omega_0 \leq 0.2$ , they are replaced by another mode, one with a “zero-frequency”. Because of the initial-value approach used here, it is difficult to determine whether the flute modes are completely stabilized during this period, or their growth rates merely fall below those of the “zero-frequency” modes. It is clear that there are at least two competing modes, and the system is never completely MHD-stable as the rotation frequency is increased to levels necessary for centrifugal confinement.

We will discuss the differences between the interchange and the new “zero-frequency” modes in terms a specific example at  $\Omega_0 = 0.3$  and for  $m = 8$ . As seen in Fig. 10, the new mode ( $\omega_r \sim 0$ ) is localized close to the plasma boundary ( $r = 1$ ), and has an eigenvalue  $\omega = (4.95 \times 10^{-2}, \sim 0)$ , whereas the interchange mode is located well within the bulk plasma with  $\omega = (8.60 \times 10^{-2}, 2.19)$ . Due to their differing localizations and the large difference in the real parts of their eigenvalues, in this particular instance we are able to (temporarily) converge, even with our initial-value approach, to one or the other mode by choosing the initial perturbation carefully. For  $t \rightarrow \infty$ , however, the interchange mode emerges as the

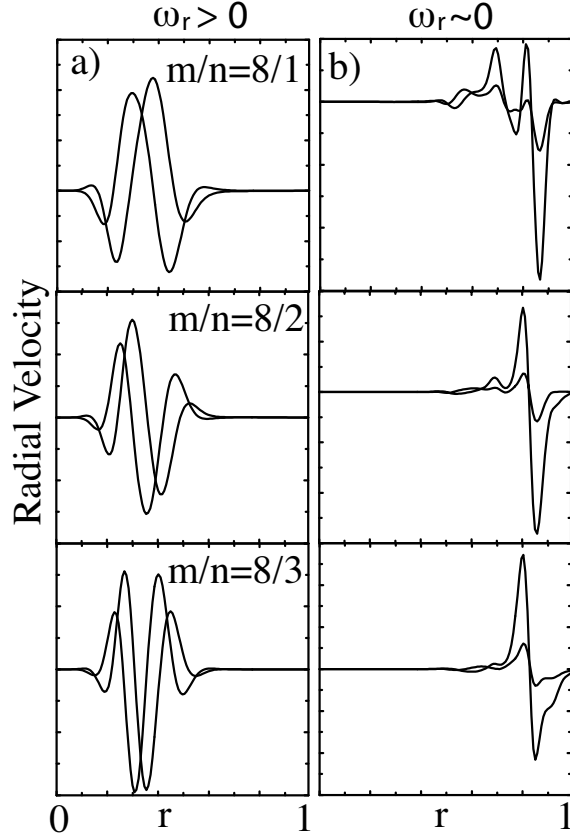


FIG. 10: The radial velocity eigenfunctions for the interchange (a) and “zero-frequency” (b) modes for  $m = 8$  at  $\Omega_0 = 0.3$  (the medium-shear case). Only three of the toroidal harmonics are shown for each. Because of rotation, the phase is complex; both the real and imaginary parts are displayed. Note that the two modes are localized at different radii.

dominant one regardless of initial conditions, and in general, only the mode with the higher growth rate can be seen (*e.g.* for  $\Omega_0 > 0.3$  for this particular equilibrium.)

A second major difference between these two modes is in their behavior along the field lines. At this moderate rotation rate, the interchange mode is still flute-like and has  $(\mathbf{B}_0 \cdot \nabla)p \simeq 0$  [Fig. 11(a)], whereas the “zero-frequency” mode exhibits a strong parallel variation [Fig. 11(b)]. Here the plasma seems to form clumps along the field lines with a short wavelength (high  $n$ ) variation. Note that this transition from interchange to zero frequency mode regime would be missed if symmetry is assumed in the toroidal (axial) direction.

It is tempting to identify the “zero-frequency” mode with either the magnetorotational (or Balbus-Hawley) instability (MRI), or the Parker (of “Sweet-Parker”) instability. The Balbus-Hawley mode is thought to be involved in anomalous angular momentum trans-

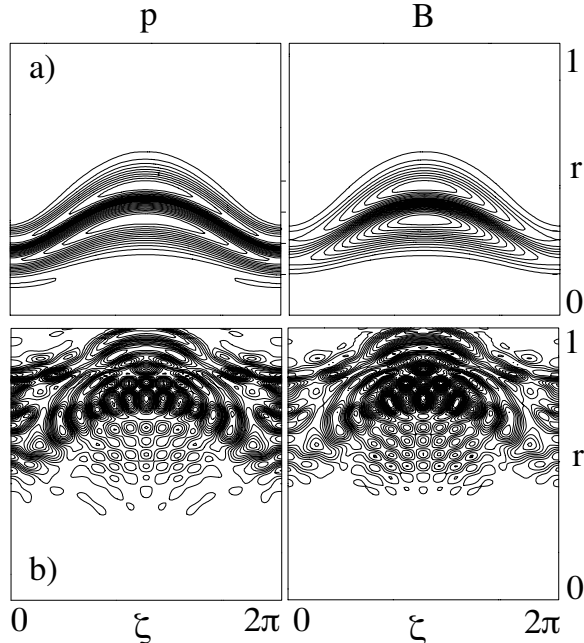


FIG. 11: The perturbed pressure and magnetic field contours in the  $(r, \zeta)$  plane for  $\Omega_0 = 0.3$  and  $m = 8$  (the medium shear case). a) The interchange mode, with  $k_{\parallel} \sim 0$ , b) the “zero-frequency” mode mode, with  $k_{\parallel} \neq 0$ . The eigenvalues are  $\omega = (8.60 \times 10^{-2}, 2.19)$ , and  $\omega = (4.95 \times 10^{-2}, \sim 0)$ , for the interchange and zero frequency modes, respectively.

port in accretion disks[13]. The Parker instability is invoked to explain the formation of nonuniformities in galactic disks[14]. The reader is referred to Huang and Hassam[15] for a discussion of these modes in the present context. However, it is difficult to claim with any certainty that the mode we see is one or the other of these, since the analytic discussions tend to be local and assume poloidal symmetry. The fact that we see a real frequency that is nearly zero ( $\omega_r \sim 0$ ) even for finite poloidal mode numbers ( $m > 0$ ) is intriguing and confusing at the same time. Since the eigenfunctions are localized in the high-shear layer, another possibility here is the shear-driven Kelvin-Helmholtz (KH) mode, but we will leave the actual identification of these modes to a later work and continue referring to them as “zero-frequency” modes here. We also note here that the “zero-frequency” mode persists at low- $\beta$ , although with reduced growth rates.

Not surprisingly, the most optimistic stability results are obtained with the high-shear profile (d) of Fig. 3, as shown in Fig. 12. All unstable interchange modes are shear-stabilized in the sense that their growth rates fall below those of the zero-frequency modes for  $\Omega_0 >$

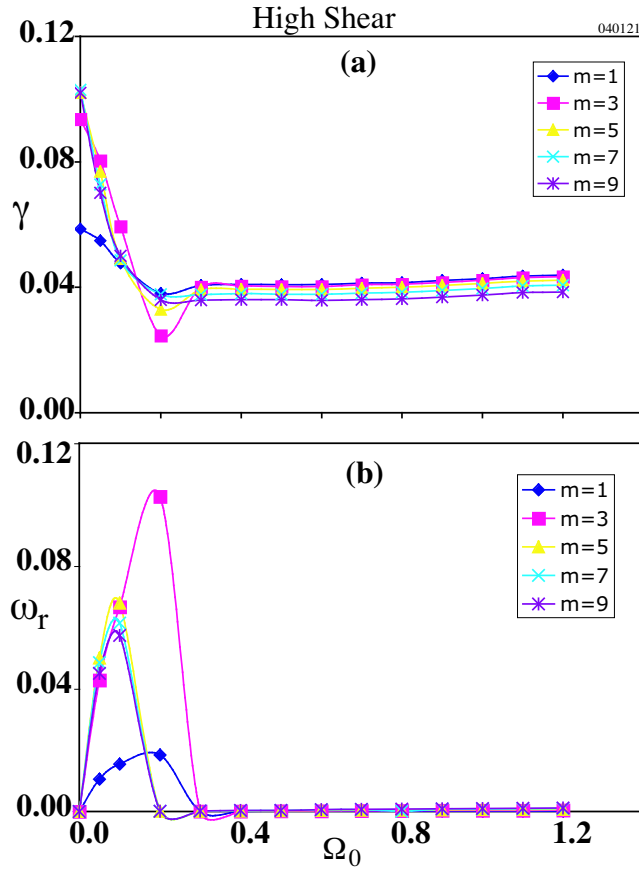


FIG. 12: The growth rate (a), and the real frequency (b), of the unstable modes as a function of rotation frequency for the high-shear profile (d) of Fig. 3. Only odd-numbered modes are shown.

0.3. They do not reappear at higher rotation rates, as they have done the with lower shear cases above. Again, it is difficult to determine with our initial value approach if the interchange modes have been completely stabilized or merely weakened enough for other modes to become dominant in the system. In the next section on pure  $\theta$ -pinch stability calculations, we will revisit this question. However, an important conclusion of this section is that, regardless of what happens to the interchange modes with strong flow-shear, there seem to be unstable MHD modes for all rotation rates and for all rotation frequency profiles examined.

## B. Stability of a $\theta$ -pinch with rotation

Because of the absence of axial symmetry, all toroidal mode numbers ( $n$ ) are coupled in the mirror calculations discussed in the previous subsection, making it difficult to understand the nature of the unstable modes with finite parallel wave numbers. Here we remove the mirror fields and revert to the simpler geometry of a  $\theta$ -pinch, which has both poloidal and toroidal symmetry. (Note that symmetry assumptions apply to the equilibrium states, but not necessarily to the stability calculations.) Thus, an important advantage of this geometry is that we will be able to look at stability of pairs of poloidal and toroidal mode numbers,  $(m, n)$ , instead of a given  $m$  with coupled toroidal harmonics as in the previous section. A couple of important points need to be kept in mind. Since a static  $\theta$ -pinch is neutrally stable, any MHD instability observed here will be driven by rotation. Also, without the destabilizing influence of the mirror fields, results here will tend to be more optimistic than in a mirror.

In Fig. 13, we plot the growth rates of unstable modes in the two-dimensional wave-number space  $(m, n)$  using bubble charts, with the size of the bubble being directly proportional to the growth rate. We tried to maintain a uniform scaling so that the growth rates can be compared within each figure and also among different figures in this subsection. The figure has four panels, corresponding to four different rotation rates. The frequency profile is  $\Omega(x(r)) = \Omega_0 f_2(x)$ , with  $f_2(x)$  given by Eq. 19, using  $\lambda = 2$ . The insets show evolution of the pressure and density profiles, which become hollow due to centrifugal forces for  $\Omega_0 \geq 0.3$ . Here the  $m$ -axis ( $n = 0$ ) corresponds to pure interchange modes with  $k_{\parallel} = 0$ . Similarly, the  $n$ -axis would represent the MRI, Parker, or KH modes, with a symmetry assumption in the poloidal direction, as it is commonly done in the literature. Thus, in the first panel ( $\Omega_0 = 0.1$ ), there are only weakly unstable interchange modes. As  $\Omega_0$  increases, we see other modes with  $n > 0$  become unstable. For  $\Omega_0 = 0.5$  (the last panel), where the centrifugal forces have effectively removed the plasma from the axis, a large number of modes with finite  $(m, n)$  are robustly unstable. For reference, the  $m/n = 2/3$  mode, which has the largest

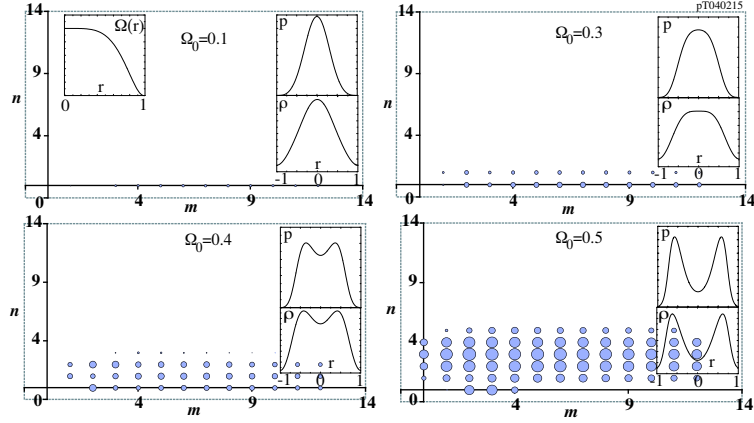


FIG. 13: The growth rates  $\gamma(m, n)$  plotted as bubble charts in a  $\theta$ -pinch with a medium-shear rotation profile, shown at four different rotation frequencies. The frequency profile is  $\Omega(x(r)) = \Omega_0 f_2$ , with  $f_2$  given by Eq. 19, using  $\lambda = 2$ . The insets show  $\Omega$ , pressure, and density. Note that both the pressure and density profiles become hollow at high rotation rates due to centrifugal forces.

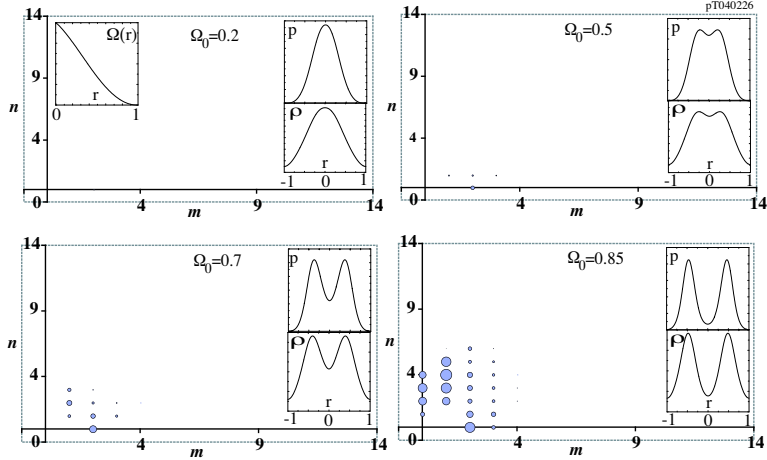


FIG. 14: Same as Fig. 13, except with higher shear ( $\lambda = 0.6$ ).

“bubble” at  $\Omega_0 = 0.5$ , has a growth rate of  $\gamma = 0.233$ . The Figure was produced by scanning in the range  $0 \leq m \leq 12$ , and  $0 \leq n \leq 12$ . Thus, there does not appear to be any unstable modes for  $n > 5$ , but the range in  $m$  has apparently been truncated prematurely.

Repeating the calculations with higher shear ( $\lambda = 0.6$  in Eq. 19), we obtain the more optimistic results shown in Fig. 14. The unstable region has shrunk significantly, and there are no unstable modes for  $m > 4$ , or  $n > 6$ . However, the  $m = 2$  interchange, and the  $m = 1, n = 3, 4, 5$  mixed modes still have significant growth rates ( $\gamma(1, 4) = 0.186$ ).

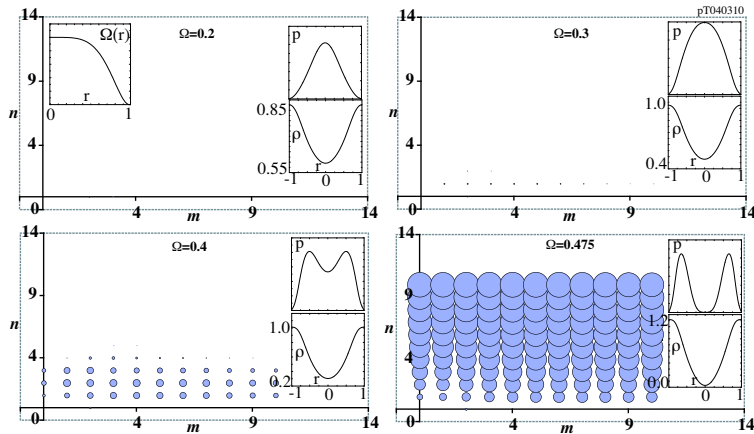


FIG. 15: Same as Fig. 13, except with an inverted density profile ( $\partial\rho/\partial r > 0$ ).

The final example, shown in Fig. 15, uses medium flow-shear coupled with an inverted density profile,  $\partial\rho/\partial r > 0$ . With the density gradients now parallel to the effective “g” of centrifugal forces, the interchange modes ( $n = 0$ ) are now essentially all stable. (There continues to be a weak  $m/n = 2/0$  mode, the origin of which is unknown.) Unfortunately, there is a full spectrum of  $n \geq 1$  modes robustly unstable, especially when the rotation rate is high enough for the centrifugal forces to evacuate the region around the axis. Note that the scan is truncated in both the  $m$  and  $n$  directions and does not show the full size of the unstable space.

All the equilibria in this subsection had  $\beta = 10\%$ . Similar results are obtained at lower  $\beta$ , since the instability drive is completely due to rotation. Without the mirror fields, the ambient field strength in these  $\theta$ -pinch calculations is of the order  $\sim 0.1$ . Thus, the Alfvén Mach number is quite high, approaching  $M_A \sim 1$  for the highest rotation cases shown in the figures above.

## V. SUMMARY AND DISCUSSION

We have examined the equilibrium and stability of rotating plasmas in a mirror geometry using a single fluid MHD model. Simple arguments in ideal MHD equilibrium show that

the rotation velocity has to be supersonic for centrifugal forces to play a significant role in confinement. Since the sound waves play a dominant role in removing mass density gradients along field lines, intuitively it is clear that any process that generates such gradients has to operate on a faster time scale than the sound waves. Of course, there is also an upper limit on rotation rates imposed by radial force balance. We showed that combining these two requirements leads  $1 < M_s^2 < (1 - \beta_0)/\beta_0$ , where  $\beta_0$  is a measure of the plasma  $\beta$ , as a condition for effective centrifugal confinement. Looking in this range of parameters, we found equilibrium states that are partially insulated from the mirror throats by centrifugal forces. In these detached states, the plasma mass concentrates at the symmetry plane between the mirror ends, forming a ring-like structure that encircles the mirror axis. Because of rapid heat conduction along the field lines, however, the temperature remains a flux function, connecting the center to the end points. Thus, centrifugal confinement tends to be a confinement of mass but not energy.

A non-rotating mirror is unstable to the well-known flute (interchange) modes. Rotation itself has a further destabilizing influence on these modes because of the centrifugal forces it generates. The shear in the rotation profile, however, is stabilizing, as demonstrated by the extensive work of the Maryland group on this topic. In ideal MHD, however, rotation frequency has to be a flux function in order to avoid twisting and winding of the field lines; that is, it cannot have shear in the parallel direction. Thus, a poloidal shear-flow, while effective in stabilizing modes with finite  $\mathbf{k}_\perp = m\nabla\theta$  such as the interchange modes, cannot influence those with  $k_\perp = 0$  but finite  $k_\parallel$ . Consequently, as shear-flow removes or weakens the interchange modes, they are replaced by modes with  $k_\parallel \neq 0$ , such as the Balbus-Hawley, Parker, or Kelvin-Helmholtz instabilities, all of which can be driven by rotation. In our calculations, we have not been able to remove all of these competing modes simultaneously; thus, our rotating mirror equilibria, *i.e.* the detached states, are always unstable to one or more of these ideal MHD instabilities.

To provide further support to these stability calculations in mirror geometry, we also looked at rotating  $\theta$ -pinch equilibria, which are known to be unstable. Again using a

variety of rotation profiles, we showed that these configurations have a wide spectrum of unstable ideal MHD modes. As with mirror calculations, it was possible to stabilize the flute modes ( $n = 0$ ), this time using an inverted density profile, but not without strongly destabilizing a large number of other modes with  $n > 0$ .

In conclusion, despite promising equilibrium calculations that led to well-formed detached states, our stability calculations have consistently yielded negative results - there is no MHD stability at rotation rates required for centrifugal confinement. Moreover, since they are ideally unstable, these detached states cannot be “relaxed states” in a variational sense. However, our work is by no means meant to be the last word on the subject. First of all, our stability calculations have all been linear. It is possible that some of these modes nonlinearly saturate at small amplitudes, although with growth rates of the order of  $0.1/\tau_A$ , this scenario does not look likely. Secondly, it is possible that some two-fluid or finite-larmor-radius effects might be stabilizing. We intend to look at both these possibilities in the future as time permits.

## VI. ACKNOWLEDGMENTS

The author acknowledges a number of useful discussions with B. Breizman and is grateful to him for sharing his notes on the Parker instability. The inverted-density calculations were also his suggestion. The author is also grateful to V. Wong for correcting a mistake in his understanding of flux coordinates. This work was supported by the U.S. Department of Energy Contract No. DE-FG03-96ER-54346.

- 
- [1] E. Hameiri, *Phys. Fluids* **26**, 230 (1983).
- [2] A. Bhattacharjee, *Theory of Fusion Plasmas* (Editrice Compositori, Bologna, (1987) ), p. 47.
- [3] B. Lehnert, *Nucl. Fusion* **11**, 485 (1971).
- [4] A. B. Hassam, *Comments Plasma Phys. Controlled Fusion* **18**, 275 (1997).
- [5] A. B. Hassam, *Phys. Plasmas* **6**, 3738 (1999).
- [6] Y.-M. Huang and A. B. Hassam, *Phys. Rev. Lett.* **87**, 235002 (2001).
- [7] R. F. Ellis, A. B. Hassam, S. Messer, and B. R. Osborn, *Phys. Plasmas* **8**, 2057 (2001).
- [8] B. R. Osborn, R. F. Ellis, and A. B. Hassam, *Phys. Fluids* **10**, 2389 (2003).
- [9] Z. Yoshida and S. M. Mahajan, *Phys. Rev. Lett.* **88**, 095001 (2002).
- [10] S. M. Mahajan and Z. Yoshida, *Phys. Rev. Lett.* **81**, 4863 (1998).
- [11] A. Y. Aydemir and D. C. Barnes, *J. Comput. Phys.* **53**, 100 (1984).
- [12] R. D. Hazeltine, S. M. Mahajan, P. M. Valanju, and H. Queveda (Private communication) (2003); see also IFSR-984 at <http://peaches.ph.utexas.edu/ifs/reports2003.html>
- [13] S. A. Balbus and J. F. Hawley, *Rev. Mod. Phys.* **70**, 1 (1998).
- [14] E. N. Parker, *Astrophys. J.* **145**, 811 (1966).
- [15] Y.-M. Huang and A. B. Hassam, *Phys. Plasmas* **10**, 204 (2003).